# Resonance Overlap of Tesseral Harmonics in the Artifical Earth Satellite Problem

T. A. Ely and K. C. Howell
School of Aeronautics and Astronautics
Purdue University
West Lafayette, Indiana

1995 SIAM Dynamical Systems Conference
Snowbird, Utah
May 21-24, 1995

# RESONANCE OVERLAP OF TESSERAL HARMONICS IN THE ARTIFICIAL EARTH SATELLITE PROBLEM

**Todd A. Ely[1] and Kathleen C. Howell[2]**

Historically, orbits with mean motions resonant with the Earth's rotation rate have been popular choices for Earth satellites because of their near-repeating groundtracks. Of increasing interest are eccentric and inclined resonant orbits. This paper addresses the long term dynamics of satellite orbits in this class. The results demonstrate that as the orbits eccentricity grows the resonance islands associated with individual long-period tesseral (longitude dependent) geopotential harmonics increase their size and interaction. Eventually, the resonance islands overlap and break up invariant tori lying between them, thus producing regions of chaos. Additionally, at a 'critical' inclination another resonance with zonal (longitude independent) geopotential harmonics must be considered. At that value of inclination, the tesserals and long-period zonal harmonics overlap. The resonance overlap problem (for both the tesseral and zonal harmonics) can be posed as a 2 degree of freedom autonomous Hamiltonian system, thus the Poincaré section proves useful in understanding the phase space. The analysis in this study has goals that are threefold: to examine the mechanisms causing these orbits to become chaotic; to characterize the regions of phase space where these orbits exist; and, finally, to analyze the features of the motion.

## Introduction

Eccentric and inclined orbits with near-repeating groundtracks result in satellite trajectories that return to the same region periodically throughout the day and spend a majority of the flight over one hemisphere of the Earth. Because of these features many communications, scientific, and military satellite missions have employed this class of orbit for operational use. The 12 hr Molniya orbit, for example, has been used extensively by the former Soviet Union for their domestic communications system; with at least 110 satellites in this system employing these orbits since 1965.[1] Additional example missions employing inclined, eccentric, synchronous orbits include: the Combined Release and Radiation Effects satellite, launched in the early 1990's to investigate the solar magnetosphere;[2] the planned Archimedes satellite, intended to provide telecommunications over the European continent;[3] and the planned Ellipso satellite constellation, intended to provide mobile ground communications services.[4] Unlike more benign geostationary orbits, this class of synchronous orbits is dynamically very complex. In this orbital regime, geopotential tesseral (dependent on Earth longitude) harmonics can interact to produce multiple resonances that result in significant nonlinear motions compared to nearby orbits without resonances. It is found that the orbital elements exhibit relatively large amplitude oscillations that diverge markedly from neighboring trajectories -- they are chaotic. Furthermore, mission effectiveness dictates that these orbits be maintained at a minimum maneuver cost. Both requirements, geographic and minimum cost, translate into a need for precise orbit control of trajectories that can experience significant nonlinearities over the lifetime of a vehicle. This paper addresses the long term dynamics of satellite orbits with multiple resonances. In particular, this study is directed toward examining the mechanisms causing these orbits to become chaotic; characterizing the regions of phase space where these orbits exist and regions in which such behavior does not appear; and, finally, analyzing the features of the motion. Future efforts will investigate the impact of these chaotic motions on the orbit control process.

---

[1] Graduate Student, School of Aeronautics and Astronautics, Purdue University, 1282 Grissom Hall, West Lafayette, Indiana 47907-1282.

[2] Associate Professor, School of Aeronautics and Astronautics, Purdue University, 1282 Grissom Hall, West Lafayette, Indiana 47907-1282.

Numerous researchers have endeavored to understand the long term evolution of resonant Earth orbits. In the case of an isolated resonance, a thorough understanding of the orbit behavior is known. Garfinkel[5] has labeled this the Ideal Resonance Problem (IRP). Using canonical perturbation theory he was able to characterize a satellite's motion in near resonance to be similar to that of a simple pendulum. Near the exact resonance the satellite 'librates' around a stable fixed point (a point fixed over the Earth) and further away the satellite 'circulates' around the Earth. Gedeon[6] and, later, Lane[7] conducted extensive analytical investigations to characterize orbits that are in resonance with any specified, isolated tesseral harmonic. Their results corroborate Garfinkel's conclusions, and offer generalizations to a larger class of orbits (although isolated resonance must still be maintained). An additional resonance of particular interest is at the critical inclination. At this inclination, perigee exists as a fixed point (at other inclinations perigee exhibits secular behavior), and geopotential zonal (independent of Earth longitude) harmonics become important. A survey paper by Jupp[8] provides an extensive set of references on the history of this subject, and describes the resonant structures that can be found at critical inclination. Hough[9] also identifies these structures, and determines their regions of applicability. Results from Jupp and Hough show the critical inclination to have isolated resonance structures that do not fall within the prescriptions of the IRP result. There are six types of resonances that can occur at the critical inclination -- not all of which are physically possible. The structures depend on eccentricity and semi-major axis, and exist because of the interaction of zonal harmonic terms in the geopotential as well as the luni-solar effects. However, the analyses by Jupp and Hough still consider only the isolated resonance case (i.e., no interaction with tesseral harmonics).

Much has been published on the IRP and its many variations, however, fewer investigations have examined multiple interacting resonances. Relatively recent results from nonlinear dynamical systems theory has shed light on this problem. Indeed, there is much literature on the interacting resonance problem for natural celestial systems. But, for the artificial satellite problem, only a small number of published results are known to the authors. Frazier[2] conducted an exhaustive study of highly eccentric resonant orbits. He uncovered numerical evidence supporting the existence of chaotic resonant Earth orbits, but did not characterize these orbits. Delhaise and Henrard[10] applied semi-numerical techniques to study the interaction between a resonant satellite's mean motion and critical inclination. They found that second order oblateness effects can interact with resonant tesseral harmonics at the critical inclination to produce chaotic regions between libration and circulation (inclination versus perigee). Their study is specific to the critical inclination class of resonant orbits. Fieger[1] compared trajectory predictions using semianalytic theory applied to arcs of real data for highly eccentric orbits. Semianalytic theory numerically integrates mean element sets (long term dynamics); this approach is consistent with the methodology used in this study. His results show good agreement between the semianalytic predictions and the real data. The present effort considers 12 hr and 8 hr resonant orbits with significant eccentricities and inclinations. A satellite with a 12 hr period returns *roughly* to the same spot over the Earth twice a day and an 8 hr orbit returns three times a day. In other words, the satellite's mean motion is *nearly resonant* (or *nearly commensurate*) with the Earth's rotation rate. A previous work by [11] considered the 24 hr resonant orbit. Additionally, resonance overlap at critical inclination is also considered. To avoid drag perturbations induced by the Earth atmosphere the selected range of orbits remains outside of the atmosphere; eccentricities below .73 prove sufficient for the 12 hr orbits, and below .65 for the 8 hr orbits.

## Analysis

This analysis is structured in terms of an analytical investigation and a numerical one. The goal of the analytical study is to arrive at first order criteria for predicting conditions sufficient for chaos to occur. In the numerical investigation, orbits are numerically integrated with the goal of corroborating the analytical predictions by observing the relatively extreme divergence of neighboring trajectories (a qualitative indicator of chaos). However, this observation is not sufficient to conclude that an orbit is chaotic. The problem in this study can be posed as an autonomous 2-Degree-of-Freedom (2-DOF) Hamiltonian system, thus Poincaré sections prove useful in determining phase space regions of regular and chaotic motion. When possible, the sections are constructed using an efficient symplectic mapping technique, otherwise numerical integration is employed for the construction. Finally, comparisons between the trajectory plots and the sections are offered.

## Model Formulation

*Inverse Square Gravity Field.* In identifying an appropriate dynamical model, it is essential to recognize the many forces that perturb a satellite orbit from a nominal elliptical Keplerian path and can, over the lifetime of a satellite, cause significant nonlinear deviations. The model formulation first introduces the integrable problem of a satellite in orbit about a spherical Earth, later the model is generalized to include perturbations from a non-spherical Earth. A nominal orbit is obtained by modeling the Earth as a sphere and the orbiting satellite as an infinitesimal mass. For this first approximation, a Newtonian inverse square gravity field is sufficient. Figure 1 depicts the geometry of motion resulting from this model. The XYZ reference frame is inertially fixed with origin at the center of the Earth. The Earth's equator defines the XY plane, and the Z axis lies along the poles (North is positive). The Earth's mean rotation rate is counterclockwise and is denoted as $\dot{\theta}_e$. The orbit is an ellipse that lies on a plane with the Earth acting as a focus of the ellipse (hence the orbital plane passes through the center of the Earth, as well). A counterclockwise motion of the satellite along the orbit is called prograde, and clockwise motion is called retrograde. The orientation of the orbital plane with respect to the Earth's equatorial plane can be defined using two angles. The first is the right ascension of the ascending node $\Omega$, it defines the angle from the X-axis to the line of intersection (the 'line of nodes') between the equatorial and orbital plane. Furthermore, the angle is made unique by associating it with the point of intersection corresponding to the satellite ascending through the equatorial plane. The inclination $i$ defines the relative angle between the equatorial and orbital plane, and positive is North. Two more angles are needed to specify the position of the satellite in the orbit for any given time. Perigee (or generically periapsis) is defined as the point of closest approach between the satellite and the Earth; the argument of perigee $\omega$ defines the angle along the orbit plane from the ascending node to perigee. The true anomaly $\nu$ completes the position identification. It defines the angle between the position vector of the satellite $\bar{r}$ and perigee, and is in the orbital plane. For the purposes of this investigation the mean anomaly $M$ proves more useful than the true anomaly. It is an angle that defines the mean position of the satellite over one rotational period. Finally, the elliptic shape of the orbit is defined with the usual conic section quantities: the semi-major axis $a$ specifies the size of the ellipse and eccentricity $e$ specifies the deviation away from a circle ($0 \le e < 1$ with $e = 0$ corresponding to a circular orbit). The preceding variables identify the *classical* orbital elements $(a, e, i, \Omega, \omega, M)$ that, assuming an inverse square gravity field, completely specify the orientation of the orbital plane in space, the size and shape of the orbit, and the position of the satellite in the orbit. This model is conservative and completely integrable, thus it can be cast in the form of a Hamiltonian system.

The previous discussion introduced a 6-dimensional (6-D) model of a satellite in orbit about a spherical Earth. The coordinates specifying the satellite position are all constant except for the mean anomaly $M$ which varies linearly with time according to,

$$M = n(t - \tau), \quad n = \sqrt{\frac{\mu}{a}}, \tag{1a,b}$$

where $n$ is the satellite's mean motion, $t$ is time, $\tau$ is the time of first perigee passage, and $\mu = GM_E$ is the Earth's reduced mass ($G$ is the Universal Gravitational constant and $M_E$ is the mass of the Earth). Recall that the class of orbits considered are nearly commensurate with the Earth's rotation rate. Hence the resonance relation $n = s\dot{\theta}_e$ ($s$ is an integer) and Eq. (1b) together identify specific semi-major axes for 12 hr and 8 hr orbits. Specifically, a semi-major axis of 26,610 km corresponds to a 12 hr period orbit ($s$

= 2), and 20,307 km to an 8 hr period orbit (s = 3). Now, the total energy (equivalent to the Hamiltonian) for this system is written,

$$H_o = -\frac{\mu}{2a}. \tag{2}$$

To actually use this equation in a Hamiltonian treatment requires introduction of action/angle pairs. Goldstein[12] performs the explicit construction that transforms the classical coordinates into action/angle pairs with the results shown in Table 1.

**Table 1**

**Action/Angle Pairs for the Inverse Square Problem**

| Action | Angle |
|---|---|
| $L = \sqrt{\mu a}$ | $l = M$ |
| $G = L\sqrt{1-e^2}$ | $g = \omega$ |
| $H = G\cos i$ | $h = \Omega$ |

Using this set of variables (often called the Delaunay variables) the nominal inverse square problem can be cast in a form capable of being analyzed using tools from the Hamiltonian formalism. Using these action/angles, Eq. (2) can be rewritten in a more appropriate form as,

$$H_o = -\frac{\mu^2}{2L^2}. \tag{3}$$

Equation (3) represents a 1-DOF integrable Hamiltonian system in $(L,l) \Leftrightarrow (a,M)$, with ignorable action/angle pairs $(G,g)$ and $(H,h)$.

*Perturbations.* Recall that an integrable Hamiltonian expressed in action/angle pairs induces motion on a torus. A perturbation to the Hamiltonian may destroy the integrability of the system, if the perturbation and appropriate initial conditions introduce resonances between system frequencies. The general form of an *n*-DOF smooth Hamiltonian system ($n > 1$) expressed in actions *J* and angle coordinates $\theta$ with the integrable term $H_o$ being perturbed by the term $\varepsilon H_1$ is written,

$$H = H_o(J) + \varepsilon H_1(J,\theta). \tag{4}$$

In nonlinear oscillatory problems (such as the orbit problem) resonance occurs when initial conditions produce unperturbed angular frequencies that are nearly commensurate. The frequencies combine linearly to produce slow, long-period motions ($r \cdot \omega_o \equiv r \cdot \partial H_o / \partial J \approx 0$, where *r* is an *n*-vector of coefficients and $\omega_o$ are the unperturbed frequencies). The resonant terms of the perturbation $\varepsilon H_1$ (i.e., those with the long-period angular rate dependencies of the form $r \cdot \omega_o$) are intrinsic to the motion and cannot be removed by a transformation. More precisely, there does not exist a near-identity, differentiable change of coordinates from the solution manifold of the unperturbed system to the solution manifold of the perturbed system (i.e., the 'zero divisor' problem). Conversely, the presence of only short period terms (and no resonant terms) in the perturbing Hamiltonian implies that a transformation can be found from the unperturbed manifold to the perturbed manifold, a conclusion justified by the KAM Theorem. Trajectories lying on these manifolds eventually separate with time; but they *always* remain close to each other in the sense that their associated manifolds are $O(\varepsilon)$-close. This is not necessarily true with resonance. Therefore, in determining the long-term *nature* of the response to an oscillatory system, it is sufficient to consider only the resonant terms. The short period effects can be superimposed later to obtain a complete quantitative response that is accurate over *finite* time scales.

*Geopotential Expansion.* The inverse square field is only a first approximation for determining motion of a satellite about the Earth; a more accurate model must account for the Earth's non-spherical effects. These are perturbations to the inverse square field, and can introduce resonances that destroy the integrability of the system in Eq. (3). In general, Earth's geopotential satisfies Laplace's equation in spherical coordinates. Furthermore, a Legendre series expansion to this problem can be obtained, and then transformed into the classical coordinate system. One solution found by Kaula[13] produces the following Hamiltonian,

$$H = -\frac{\mu}{2a} + \sum_{l=2}^{\infty}\sum_{m=0}^{l}\sum_{p=0}^{l}\sum_{q=-\infty}^{\infty} V_{lmpq}(a, e, i, \Omega, \omega, M, \theta_e), \tag{5}$$

where $V_{lmpq}$ is an individual harmonic term, i.e.,

$$V_{lmpq} = -\frac{\mu R_e^l}{a^{l+1}} F_{lmp}(i) G_{lpq}(e) J_{lm} \cos\psi_{lmpq}(\Omega, \omega, M, \theta_e). \tag{6}$$

Again, the classical orbital elements $(a, e, i, \Omega, \omega, M)$ produce a 6 dimensional (6-D) phase space, $R_e$ is the Earth radius, $\theta_e$ is the mean Greenwich Sidereal angle ( = (mean Earth rotation rate × time past epoch) + initial Earth longitude), $F_{lmp}(i)$ and $G_{lpq}(e)$ are the inclination and eccentricity functions, respectively, defined in [13], and $J_{lm} = \sqrt{C_{lm}^2 + S_{lm}^2}$ is the unnormalized coefficient corresponding to the tesseral harmonic of degree $l$ and order $m$. Note that $G_{lpq}(e)$ is written explicitly as a power series and, in the subsequent analysis, terms to the order $O(e^{44})$ are retained. This is consistent with a first order analysis, and the range of eccentricities investigated. A note on evaluating the function $G_{lpq}(e)$ is in order. In subsequent analysis it is found that the essential features of the dynamics can be discerned from only 3 to 5 harmonic terms. Because this is a small number, the authors employed an explicit expansion of $G_{lpq}(e)$ (obtained by symbolic manipulation using *Mathematica*®) rather than implementing a recursive formulation. For the purposes of the present paper, this approach is more efficient. The angle argument represents the following function,

$$\psi_{lmpq} = (l - 2p + q - \frac{m}{s})(M + \omega) + m\left\{\frac{1}{s}(M + \omega) - (\theta_e - \Omega) - \lambda_{lm}\right\} - q\omega, \tag{7}$$

and,

$$\lambda_{lm} = \begin{cases} \frac{1}{m}\tan^{-1}\left(\frac{S_{lm}}{C_{lm}}\right) & l - m \text{ even} \\ \frac{1}{m}\tan^{-1}\left(\frac{C_{lm}}{-S_{lm}}\right) & l - m \text{ odd} \end{cases}, \tag{8}$$

where $\lambda_{lm}$ is the phase angle associated with $J_{lm}$, and $s$ is the integer nearest the ratio: satellite mean motion over Earth rotation rate.

*Effects of an Oblate Earth.* In general the tesseral harmonic terms are dependent on the Earth longitude, hence the appearance of $\theta_e$ in Eq. (7), when the order $m$ is not equal to zero. However, for harmonic terms with $m$ equal to zero the dependence on Earth longitude is lost, and these are the *zonal* harmonics. The first set of zonal terms with coefficient $J_2$ (the $m = 0$ identifier is dropped) derive from the Earth's oblate spheroid shape, and are the largest effects beyond the inverse square field. For this reason they are considered first order terms. The harmonic terms dependent on $J_2$ will have an index of the form $\{(l, m, p, q)\} = \{(2,0,0,q), (2,0,1,q), (2,0,2,q)\}$; these will be either secular (no dependence on mean anomaly) or short period (a multiple of the mean anomaly). The term $V_{2010}$ introduces first order secular changes to the orientation of the orbit $(\Omega, \omega)$ and to the mean anomaly $M$. These secular effects prove to be essential in the subsequent analysis. On the other hand, the remaining $J_2$ short period terms have no average affect on the orbital elements for finite time spans longer than the orbital period. Since this study is concerned with long-term dynamics, these short period terms are not included in the analysis. Now, the next largest coefficient $J_{lm}$ is several orders of magnitude smaller than $J_2$, thus, typically, the remaining terms may be considered of second order. However, as the orbital frequencies become commensurate with the Earth's rotation rate, resonances are introduced that increase the order, and importance, of some of these terms.

*Critical Tesseral Harmonics.* Certain long period terms in the geopotential expansion can introduce resonances that lead to nonintegrability of the perturbed system. For the 12 hr and 8 hr orbits considered in this work, the critical (or resonant) tesseral harmonics ($m \neq 0$) are found by retaining terms in Eq. (5) that have angular rates $\dot{\psi}_{lmpq}$ near zero. This results in the following condition on the expansion indices,

$$l - 2p + q - \frac{m}{s} = 0. \tag{9}$$

The expression in Eq. (7) reduces to $\psi_{lmpq} = m(\lambda - \lambda_{lm}) - q\omega$ where,

$$\lambda \equiv \frac{1}{s}(M + \omega) - (\theta_e - \Omega), \tag{10}$$

is the stroboscopic mean node. In the notation of Eq. (4), the condition $\dot{\psi}_{lmpq} = r \cdot \omega_o \approx 0$ yields $r = (m, -q)$ and $\omega_o = (\dot{\lambda}, \dot{\omega})$. Applying the condition in Eq. (9) to the 12 hr and 8 hr resonant orbits yields the critical harmonics used in the analysis that are listed in Table 2. Other critical harmonics exist, but those in Table 2 are the primary resonance terms that affect the qualitative nature of the motion.

**Table 2**

**PRIMARY CRITICAL HARMONICS FOR THE 12 HR AND 8 HR RESONANT ORBITS**

| | | | | | |
|---|---|---|---|---|---|
| **12 hr Orbits** | | $V_{220-1}$ | $V_{3210}$ | $V_{2211}$ | |
| **8 hr Orbits** | $V_{330-2}$ | $V_{431-1}$ | $V_{3310}$ | $V_{4321}$ | $V_{3322}$ |

It is found that the size of these resonant terms depends on eccentricity and inclination. At certain values of eccentricity and inclination the resonances can overlap to produce chaotic motions.

*Critical Inclination.* Recall that the $V_{2010}$ term introduced secular changes to perigee. The secular rate is dependent on the inclination, and is the dominant effect on perigee until a *critical* *inclination* is reached. When the inclination reaches $i = \cos^{-1} \pm 1/\sqrt{5} = (63.4°, 116.6°)$ the secular rate goes to zero. Near these equilibrium values higher order, long-period terms (i.e. resonant terms) can dominate the response of perigee. These terms are zonal harmonics ($m = 0$) that are independent of mean anomaly, thus implying $q = 2p - l$. Orbits that have a mean motion commensurate with the Earth's rotation rate and with inclination near the critical value can encounter resonance overlap between the long-period zonal and tesseral harmonics. Again, just as with an overlap of the tesseral harmonics, chaotic motion can result from this overlap. This study initially considers the impact of $J_3$ and $J_4$ long period zonals and a $J_4$ secular term. The relevant harmonic terms from Eq. (5) are listed in Table 3.

**Table 3**

**Long Period and Secular Zonal Harmonics at Critical Inclination**

| | | | |
|---|---|---|---|
| $J_3$ | $V_{301-1}$ | $V_{3021}$ | |
| $J_4$ | $V_{401-2}$ | $V_{4020}$ | $V_{4032}$ |

Note that $V_{4020}$ is secular; the remaining terms are long-period with an angle dependency on perigee. There is an additional long-period/secular, 2nd order zonal term, $J_2^2$, that must be included, as well. Hough[9] discusses the procedure for arriving at this term, the form of which is given by,

$$V_{J_2^2} = -\frac{\mu^6}{L^{10}} \frac{R_e^4 J_2^2}{4} \left[ A(L, e(L,G), i(L,G,H)) \cos 2\omega + C(L, e(L,G), i(L,G,H)) \right]. \tag{11}$$

The detailed equations for $A$ and $C$ are discussed by Hough[9] and Delhaise[10].

*Complete Model.* The resulting nonlinear model, represented in the form,

$$H = -\frac{\mu}{2a} + V_{2010} + \sum_{\Re} V_{lmpq}, \tag{12}$$

contains the primary dynamical features that are required for determining resonant, long term orbit evolution. The finite set $\Re$ contains the critical harmonics involved in the summation, including those listed in Table 2, Table 3, and the $V_{J_2^2}$ term. Now, the Hamiltonian in Eq. (12) is transformed into action/angle coordinates by introducing the Delaunay elements. An additional transformation using the following generating function,

$$F_2 = \lambda I_1 + \omega I_2 + \Omega I_3 = \left\{ \frac{1}{s}(M + \omega) - (\theta_e t + \theta_{eo} - \Omega) \right\} I_1 + \omega I_2 + \Omega I_3, \tag{13}$$

reduces the system by one degree of freedom. The resulting Hamiltonian can be rewritten formally as,

$$H = -\frac{\mu^2}{2L^2} - s\dot{\theta}_e L + V_{2010}(L(I_1), e(I_1, I_2), i(I_1, I_2, I_3)) + \sum_{\Re} V_{lmpq}(L(I_1), e(I_1, I_2), i(I_1, I_2, I_3), \lambda, \omega). \tag{14}$$

Because $\Omega$ does not appear in the argument list of Eq. (14), its associated action $I_3 = L(1-e^2)^{1/2}\cos i - sL$ is ignorable and constant. The Hamiltonian in Eq. (14) is now an autonomous 2-DOF system (versus nonautonomous 3-DOF) with actions $I_1 = sL$, $I_2 = L(1-e^2)^{1/2} - L$ and associated angles $\lambda, \omega$ , respectively. Note that the original variables $L, e, i$ prove more convenient for use in later manipulations than the current actions, therefore the functional dependency on $L, e, i$ will be carried. The integrable portion of the vector field $H_o$ includes the inverse square and secular terms. The perturbation $\varepsilon H_1$ includes the critical resonant harmonic terms that perturb the integrable field, and may eliminate the integrability of the system. It is this issue that is addressed in the following analysis.

## Analytical Investigation

*Overlap of Tesseral Resonances.* Consider the angles in Eq. (14); the node $\lambda$ is slowly varying because of the near commensurability of the orbit's mean motion with the Earth's rotation rate. Perigee $\omega$ varies slowly because of Earth's oblateness. When the inclination is bounded away from the critical inclination, perigee also varies secularly to first order (the zonal harmonics do not contribute significantly to the response). Perigee appears in the expansion only when $q$ is nonzero, that is, when the orbit's eccentricity is nonzero. In essence, perigee acts as a 'detuning' parameter, that amplifies dissonance between tesseral harmonics as eccentricity increases. The size of the resonant terms in Eq. (14) are primarily affected by eccentricity, and to a lesser degree by inclination. The semi-major axis, while a variable in the coefficients, has insignificant impact in the regions of interest. The dependency on eccentricity is the key effect for determining whether two tesseral resonances will interact. As an illustration, a 24 hr orbit with negligible eccentricity and inclination reduces the number of critical harmonics in Eq. (14) to a single term, the Earth ellipticity $V_{2200}$. The source of this term stems from the elliptic shape of the Earth around the equator. This is a classic IRP (indeed, this particular resonance was the motivating problem of study for the IRP) that results in a characteristically simple response: the Earth's ellipticity bifurcates the phase space at the exact resonance producing a libration region or 'island' and a circulation region surrounding the island. This situation is depicted in Figure 2. The figure actually depicts two libration islands because the stroboscopic mean node is multiplied by two in its angular argument. As a result, the harmonic term yields two stable island centers. The response changes dramatically as eccentricity increases since the coefficients of the other critical terms (not seen in Figure 2) become nonzero. If the terms are analyzed separately, each would produce its own isolated resonance response similar to the IRP.[7] The island widths increase as eccentricity increases, and island separation decreases as inclination increases. As the libration islands grow they begin to interact more strongly. The IRP result no longer provides an accurate description of the motion because the harmonics are not isolated. The KAM theorem states that if the islands are sufficiently separated, then invariant tori (quasiperiodic trajectories) will lie between the islands. However, as the islands increase in size and move closer to each other these invariant curves break up yielding chaotic trajectories. Hence, at certain inclinations and eccentricities the KAM theorem's 'sufficiently separated island' condition is violated and trajectories between the islands become chaotic.

Estimates of isolated island locations and associated widths can be obtained using secular perturbation theory. The model considered now is defined by Eq. (10) with only a single resonant tesseral term $V_{lmpq}$ present. This is written as a 1-DOF autonomous perturbed Hamiltonian system,

$$H = H_o(L(I_1'), e(I_1', I_2'), i(I_1', I_2', I_3')) + J_{lm} H_{lmpq}(L(I_1'), e(I_1', I_2'), i(I_1', I_2', I_3')) \cos\psi_{lmpq}, \tag{15a}$$

$$= -\frac{\mu}{2L^2} - s\dot{\theta}_e L - \frac{\mu^4 R_e^2 J_2}{L^6(1-e^2)^{3/2}}\left\{\frac{3}{4}\cos^2 i - \frac{1}{4}\right\} - J_{lm}\frac{\mu^{l+2}R_e^l}{L^{2l+2}} F_{lmp}(i) G_{lpq}(e) \cos\psi_{lmpq}. \tag{15b}$$

The angle in Eqs. (15a,b) is $\psi_{lmpq}$ and its associated action is $I_1' = sL/m$. Both, $I_2' = L(1-e^2)^{1/2} - L(1-qs/m)$ and $I_3' = I_3 = L(1-e^2)^{1/2}\cos i - sL$ are now constants of the motion. The position of exact resonance is determined when the action and angular rates are zero,

$$\dot{I}_1' = -\frac{\partial}{\partial\psi_{lmpq}}\left(J_{lm} H_{lmpq}(I_1')\cos\psi_{lmpq}\right) = 0 \quad \Rightarrow \quad \psi_{lmpq} = 0, \pm\pi, \tag{16a}$$

$$\dot{\psi}_{lmpq} = \frac{\partial H}{\partial I_1'} = \frac{s}{m}\frac{\partial H}{\partial L} \approx \frac{s}{m}\frac{\partial H_o}{\partial L} = 0 \qquad \Rightarrow \quad L = L^*, \tag{16b}$$

where the symbol '*' refers to the exact resonance value. Recall that finding the derivative in Eq. (16b) requires use of the chain rule because of the dependency of $e$ and $i$ on $L$. Also, use of the chain rule requires specific values for $e$ and $i$, these are denoted by '*' as well. Now, determine a local Hamiltonian by expanding Eqs. (15a,b) around $L^*$ and retaining terms to $O(J_{lm})$. Note that $\Delta L = L - L^* = O(J_{lm}^{1/2})$[5]. The resulting Hamiltonian has the form,

$$\Delta H = -\frac{3\mu^2}{L^{*4}}\frac{\Delta L^2}{2} + J_{lm}\frac{\mu^{l+2}R_e^l}{L^{*2l+2}}\left|F_{lmp}(i^*)G_{lpq}(e^*)\right|\cos\psi_{lmpq} + O(J_{lm}^{3/2}), \tag{17a}$$

$$\equiv -G\frac{\Delta L^2}{2} + F\cos\psi_{lmpq}, \tag{17b}$$

where the angle is shifted by π if $F_{lmp}(i^*)G_{lpq}(e^*) > 0$. Equation (17b) has the same structure as a simple pendulum, hence the motion of a satellite in resonance with an isolated tesseral is equivalent to that of the pendulum. (See Figure 2.) The maximum half-width excursion of the action is given by,

$$\Delta L_{\max} = 2\sqrt{\frac{F}{G}}, \tag{18}$$

which can be converted to semi-major axis and yields the following useful expression,

$$\Delta a_{max} = \frac{4\sqrt{3}}{3}a^*\sqrt{\left(\frac{R_e}{a^*}\right)^l \left|F_{lmp}(i^*)G_{lpq}(e^*)\right| J_{lm}}\,. \tag{19}$$

Equations (16b) and (19) provide a method for determining (to first order) the relative spacing of the libration islands associated with each critical harmonic in Table 2.

A very simple way of determining the nonexistence of KAM surfaces between libration islands is to determine if the islands touch. Doing so is a clear violation of the KAM theorem's 'sufficiently separated island' condition, and, subsequently, any trajectories between the islands will be chaotic. Of course, the preceding result is inadequate to provide a realistic picture of the interaction between islands *as* they approach. Extensive analysis by many authors has revealed a variety of methods to determine conditions necessary for the break up of KAM surfaces between resonances. A simple method that more accurately estimates the onset of chaos is the 'two-thirds rule', developed by Chirikov[15] in 1979 using a combination of analytical techniques and numerical experiments, that is,

$$\frac{(\Delta I_{\max})_1 + (\Delta I_{\max})_2}{\delta I_{12}} \geq \frac{2}{3}, \tag{20}$$

where $(\Delta I_{\max})_i$ are the maximum half-widths of neighboring resonances and $\delta I_{12}$ is the distance between their centers. Equation (20) shows that if the fractional distance between centers is less than $1/3$, then the surfaces destabilize. These include the surfaces between island separatrices (circulation surfaces) and the outermost surfaces inside the separatrices (libration surfaces). As the widths of the islands grow, more libration surfaces destabilize, and, eventually, all surfaces destabilize eliminating any island structures. To apply Eq. (20), the neighboring islands must have approximately the same width. If they are significantly different, more sophisticated methods such as the renormalization technique of Escande and Doveil,[16] are necessary to determine the separation distance at destabilization.

To assess resonance separation distances in the 12 hr and 8 hr orbit problem, the critical resonance widths, as predicted by the first order theory for isolated resonances, are plotted as a function of eccentricity for a variety of inclinations. The island centers are computed using the condition in Eq. (16b) and their widths using Eq. (19). The results for the 12 hr case at three different inclinations (3°, 23°, 55°) are shown in Figure 3. The resonance widths are calculated at eccentricity increments of .01; the vertical bars represent the maximum full width of the resonance at the given eccentricity; finally, the dots in the middle are the exact resonance locations. The plots demonstrate that at all eccentricities there is insufficient separation between island centers to avoid overlap, and the islands actually lie within each other. This is an obvious violation of the KAM theorem, hence chaotic orbits are expected in these semi-major axis and inclination regimes. The width of the overlap regions begins very small then increases with eccentricity. The widths also increase with increasing inclination. Because the overlap is, for the most part, inside the isolated libration islands, it is expected that the orbits within the libration zone will be chaotic, and that outside the overlap region they will be quasiperiodic. This behavior is even expected at low eccentricities, although the chaotic regions will be smaller. For instance, at .05 eccentricity and an inclination of 23° the anticipated size of the region is 20 km. Note also that the separation distance between resonance centers decreases as the inclination increases. The decreasing distance indicates that the inclination is approaching the critical value. At the critical inclination there is no separation distance between tesseral resonances -- at that value the tesseral harmonics lose their dependency on perigee and become a function only of stroboscopic mean node. However, overlap with the long-period zonal harmonics must then be considered (this is done in a subsequent section). Figure 4 depicts overlays of the critical resonances for the 8 hr case at the three inclinations (3°, 23°, 55°). At inclinations of 23° and 55° the general behavior is similar to that of the 12 hr case, that is, the resonances always overlap and their widths grow with increasing eccentricity. However, the maximum widths are less than in the 12 hr case. Also, unlike the 12 hr case, the resonance widths decrease with increasing inclination. The island centers do have slightly larger separations, hence perigee rates are larger (but not by much). The most notable difference occurs in the plot with the inclination at 3°; the 12 hr case demonstrates overlap the 8 hr case shows none. Additional cases indicate that the islands corresponding to $V_{4321}, V_{3310}, V_{431-1}$ begin to intersect for all eccentricities at 13°. Of course, this estimate could be made sharper by using the 'two-thirds' rule or a renormalization technique.

*Overlap of Zonal and Tesseral Resonances at Critical Inclination.* If no long-period zonal harmonics are present in the dynamic model, then perigee becomes constant at the critical inclination. The tesserals coalesce into one isolated harmonic term, and, essentially, the behavior of the IRP is recovered, even at high eccentricities. Of course, the zonals are present and perigee is not constant. As the inclination nears the critical value perigee slows. Eventually, the long-period zonals and the secular term have the same order. When this occurs, the zonals produce a resonance island in the plane defined by inclination (or eccentricity) and perigee (assuming the stroboscopic node is bounded away from resonance and circulating). The behavior of this resonance is similar to the IRP example shown in Figure 2. To illustrate this behavior Figure 5 shows the critical inclination resonance due to the $J_2^2$, $J_3$, and $J_4$ zonal harmonics. The semi-major axis is in the circulation regime ($a$ = 26700 km) and the stroboscopic node $\lambda$ is set to 100°. As expected, the phase plane displays a libration island, an enclosing separatrix, and circulating orbits around the island. With all three zonals included in the simulation, there is only one libration region with a stable island center at perigee $\omega = 270^\circ$. If only $J_2^2$ and $J_4$ are included, two islands would appear with stable centers at $\omega = 0^\circ$ and 180°, and unstable equilibrium positions at 90° and 270°. Clearly, the modeled perturbations have a significant impact on the structure of the phase space. Determining if $J_2^2$, $J_3$, and $J_4$ is a sufficient set of zonals, or, if additional higher order terms are required, is a topic for further investigation. For illustration purposes this set is used in the subsequent analysis. One other cautionary note, Jupp[8] and Hough[9] both show that the IRP is not a satisfactory description of the critical inclination resonance at low eccentricities and additional analytical tools are required to analyze the resulting resonant structures. Low eccentricity, critical inclination cases are not analyzed in this work. Now, for high eccentricity, critically inclined resonant orbits the integrable phase plane shown in Figure 5 can change because a resonance overlap is encountered between the zonal and tesseral harmonics. One of the most popular eccentric orbits, the Molniya orbit, is critically inclined and has a 12 hr period. The subsequent numerical investigations consider a Molniya orbit.

## Numerical Investigation

*Numerical Integration.* To demonstrate the complex behavior suggested by the previous analysis, a satellite orbit with a nominal 12 hr period, an eccentricity of .7, and a 23° inclination was simulated. Various initial values of semi-major axes were selected near the exact 12 hr orbit (corresponding to a semi-major axis of 26601 km), and numerically integrated for 3000 days using a 5-th order Runge-Kutta algorithm. To verify numerical accuracy the Hamiltonian was also computed; as required, it remained constant to machine precision during the integration. The simulation results are shown in Figure 6. The figure shows four pairs of trajectories with each pair separated by 1 km. The top pair have initial semi-major axes near 26645 km, the bottom pair near 26580 km, and the two middle pairs near 26600 km and 26620 km, respectively. The top and bottom pair have amplitude variations on the order of 10 km with each pair displaying the same qualitative behavior. Specifically, the top pair exhibit quasiperiodic motion with similar oscillations grouped in threes, that is, roughly a three-cycle pattern. The bottom pair have quasiperiodic oscillations grouped in fours. Unlike the others, the middle two pairs do not exhibit a quasiperiodic structure at all. The amplitude variations are up to 6 times larger than those associated with the top and bottom pairs, and, within pairs, the neighboring trajectories are qualitatively different. Indeed, the pair at 26620 km diverge at around 900 days and the pair at 26600 km diverge near 2400 days. The middle pairs display a 'sensitive dependence on initial conditions' that is typical of chaotic trajectories. This sensitivity may have a direct impact on orbit control design. Chao and Schmitt[17] use first order perturbation theory to produce a result suggesting that longitudinal orbit control costs are proportional to the *square* of the semi-major axis variations. For the 6-fold increase in semi-major axis deviations seen in the chaotic trajectories, a 36-fold increase in stationkeeping costs might then be expected. Such a result would indicate the need to examine the performance of current controllers in this orbital regime and determine if enhancements might be beneficial. More numerical simulations are presented later with associated Poincaré sections.

*Poincaré Sections.* The preceding results generated by numerical integration provide useful quantitative information on the amplitudes and times scales associated with *specific* trajectories, however, they are insufficient for generalization to other regions of the phase space. To obtain a more complete understanding of the sets of initial conditions that lead to regular versus chaotic response, it is necessary to employ other tools. The 2-D Poincaré section has proven most useful for making these determinations, especially with conservative 2-DOF systems.[15] The section is constructed by selecting an energy (a constant), and then sampling the trajectory on returns to a specified value of $\omega$. The resulting section has coordinates $(\lambda, L)$, or, equivalently, $(\lambda, a)$. Periodic trajectories appear as fixed points; quasiperiodic trajectories appear as curves (invariant 2-D tori in the full phase space); and chaotic trajectories appear as a 'dusting' of points that densely fill regions of the section. For 2-DOF systems, the 2-D tori separate the 3-D energy 'volume' into distinct regions. They do so by isolating the resonance surfaces (defined by $r \cdot \omega_o = 0$; recall $r$ is an $n$-vector of coefficients and $\omega_o$ are the unperturbed frequencies). Under perturbation, the resonant surfaces break up (as well as some neighboring KAM surfaces) to produce regions of chaos. However, these regions can still be subdivided by KAM surfaces that persist under perturbation (i.e., those 'sufficiently far' from resonance). Hence, orbits in chaotic regions of the Poincaré section, but trapped between two KAM surfaces, cannot cross the surfaces to other portions of the section. For the 3-DOF case this picture changes dramatically. Since 3-D KAM tori can no longer divide a 5-D energy volume into distinct regions, they can no longer isolate the resonance surfaces either. In fact, the resonance surfaces intersect densely within the energy volume to form what is called the *Arnold web*. As before, a perturbation of the system can produce chaotic regions near the resonance surfaces, however now the KAM tori that persist do not isolate these regions. Thus, an orbit that starts in the chaotic region will eventually explore the entire energy volume (even for a vanishingly small perturbation). This process is *extremely* slow and diffusive in nature, hence its name -- Arnold diffusion. It acts primarily *along* resonance surfaces (not *across* as with resonance overlap). In weakly perturbed systems, a trajectory starting near a particular KAM surface will follow the surface for quite sometime, but eventually it will leak to other nearby KAM surfaces -- this is thin layer diffusion. Given sufficient time the trajectory can shift dramatically and explore other resonance surfaces (because of their interconnectedness) -- this is thick layer diffusion. The text by Lichtenberg and Liebermann[15] provides a thorough discussion of diffusion. It includes many detailed calculations and results for various types of diffusion including Arnold diffusion. For the present effort, the system is 2-DOF, hence a 2-D Poincaré section indicates the full range of possible motions. However, the sections are produced by a symplectic mapping (described next) that introduces an additional degree of freedom, thus consideration must be given to the possibility of resonance and diffusion when applying the method.

*Symplectic Mapping.* Because of the long time scales associated with the slow angular rates, perigee can take hundreds to many thousands of days before returning to the section. A practical concern in producing the sections is efficiently computing the intersection points. The computational scheme should quickly step through an orbit, yet accurately show its image on the section. Once found, the section should correctly depict the regular versus chaotic regions, however, it is not necessary that the trajectories used to compute the section be quantitatively exact -- qualitative accuracy is sufficient. In other words, capturing the KAM surface or, in the case of a chaotic zone, revealing no surface is the primary goal in producing the section. Whether the orbit used to make the section provides the correct position to machine precision on the $n$-th day is not critical. Fortunately, a symplectic method developed by Wisdom and Holman[18, 19] provides a very efficient, qualitatively accurate technique for computing trajectories over long intervals. Their method, based on the averaging theorem, uses the intuitive notion that fast oscillations (as compared with a system's slow, natural oscillations) have, on average, no net contribution to a system's long-term evolution. From the perspective of the KAM theorem, the fast oscillations perturb a system manifold $O(\varepsilon)$ away from the unperturbed manifold, but the manifold still persists if the fast oscillations are not in resonance with the system's other oscillations. Thus, trajectories with fast oscillations and without them are equivalent in the sense that a near-identity transformation exists which allows superposition of the system's fast motion onto the slow, long term component. Furthermore, if the system's intrinsic fast period terms can be neglected, then adding more fast oscillations should have no net effect either. The fast period terms that Wisdom and Holman choose to add represent the Fourier expansion of a periodic Dirac delta function. Augmenting the Hamiltonian with this series yields a set of differential equations that can be 'locally' integrated, and, yet, still provide, long-term nonintegrable motion quite accurately. Consider the Hamiltonian in Eq. (4), $H = H_o(J) + \varepsilon H_1(J, \theta)$, where the perturbation terms that are retained are resonant with slowly varying angles (i.e., those belonging to the set $\Re$ in Eq. (14)). Multiply the perturbation term with a periodic Dirac delta function to produce the 'map Hamiltonian',

$$H_{map} = H_o(J) + 2\pi\varepsilon\delta_{2\pi}(\Omega_m t)H_1(J,\theta) = H_o(J) + 2\pi\varepsilon\delta_{2\pi}(\Omega_m t)\sum_{r\,\varepsilon\,\Re} H_r(J)\cos(r\cdot\theta). \tag{21}$$

The function $\delta_{2\pi}(\Omega_m t)$ represents a series of periodic delta functions,

$$\delta_{2\pi}(\Omega_m t) = \sum_{n=-\infty}^{\infty}\delta(\Omega_m t - 2\pi n) = \frac{1}{2\pi} + \frac{1}{\pi}\sum_{q=1}^{\infty}\cos(q\Omega_m t), \tag{22}$$

where $\Omega_m$ ($>> r\cdot\omega_o$) is the 'fast' mapping frequency. For later use in analyzing the properties of the mapping, the individual resonance terms of $H_1(J,\theta)$ in Eq. (21) have been written in their multiply periodic Fourier expansion form $\varepsilon H_r(J)\cos(r\cdot\theta)$; where *r*, as before, is the unique vector identifying each term ($\Leftrightarrow V_{lmpq}(I_1, I_2, \lambda, \omega)$ in Eq. (14)). Expanding Eq. (21), the map Hamiltonian takes the form,

$$H_{map}(J,\theta,t) = H_o(J) + \varepsilon H_1(J,\theta) + 2\varepsilon\cos(\Omega_m t)H_1(J,\theta) + \ldots, \tag{23}$$

where the terms with a mapping frequency will average to zero in the limit as time goes to infinity (note this is not a periodic average, but an average in the limit).[15] The mapping Hamiltonian is now nonautonomous (thus not a constant), but upon averaging this Hamiltonian, the original one is recovered. The original Hamiltonian becomes an 'adiabatic invariant' of the mapping one. Apply Hamilton's equations to Eq. (21) to obtain the mapping equations of motion,

$$\dot{J} = -\frac{\partial H}{\partial\theta} = -2\pi\varepsilon\delta_{2\pi}(\Omega_m t)\frac{\partial H_1}{\partial\theta}, \tag{24a}$$

$$\dot{\theta} = \frac{\partial H}{\partial J} = \frac{\partial H_o}{\partial J} + 2\pi\varepsilon\delta_{2\pi}(\Omega_m t)\frac{\partial H_1}{\partial J}. \tag{24b}$$

The addition of the periodic delta function has rendered these differential equations 'locally' integrable. When the delta functions are not active, the system evolution is governed by the unperturbed term in Eq. (24b), hence the action $J$ is constant and the angle $\theta$ rotates at a constant rate defined by the unperturbed frequency. Integrating over the delta function, applied at times that are multiples of the mapping period $\Delta t_m = 2\pi/\Omega_m$, the perturbation produces two 'kicks'; one to the angle and one to the action. These integrations produce the following first order map that advances the orbit one mapping period from time $t_n$ to time $t_{n+1}$,

$$J_{n+1} = J_n - \frac{2\pi}{\Omega_m}\varepsilon\frac{\partial H_1(J_n,\theta_n)}{\partial\theta}, \tag{25a}$$

$$\theta_{n+1} = \theta_n + \frac{2\pi}{\Omega_m}\left(\frac{\partial H_o(J_{n+1})}{\partial J} + \varepsilon\frac{\partial H_1(J_n,\theta_n)}{\partial J}\right). \tag{25b}$$

Note that the unperturbed frequency term in Eq. (25b) contains the action at the new time $t_{n+1}$; this result retains the symplectic nature of the system.

*Mapping Properties and Implementation.* The relationship of the actions and angles in Eqs. (25a,b) to the original variables in Eq. (14), can be found by explicitly computing the transformation between variables. The near identity canonical transformation between the original and mapping variables is written,

$$S(\bar{J},\theta,t)=\bar{J}\cdot\theta+\varepsilon S_1(\bar{J},\theta,t)=\bar{J}\cdot\theta+\varepsilon S_1(\bar{J},\bar{\theta},t)+O(\varepsilon^2), \tag{26}$$

where the overbars on the actions and angles represent the variables after transformation to the averaged system (i.e., the original system). The second equality in Eq. (26) follows from $S_1(\bar{J},\theta,t)=S_1(\bar{J},\bar{\theta},t)+O(\varepsilon)$. The governing equation for $S_1(\bar{J},\bar{\theta})$ is of the form,

$$\frac{\partial S_1}{\partial t}+\omega_o(\bar{J})\cdot\frac{\partial S_1}{\partial\bar{\theta}}=-\left\{H_1(\bar{J},\bar{\theta},t)\right\}, \tag{27}$$

where $\left\{H_1(\bar{J},\bar{\theta},t)\right\}$ is the oscillatory part of the mapping Hamiltonian and $\omega_o(\bar{J})\equiv\partial H_o/\partial\bar{J}$. The oscillatory portion is found by averaging $H_{map}(J,\theta,t)$ over time by one mapping step $2\pi/\Omega_m$ while holding $\bar{J},\bar{\theta}$ constant (valid for $\Omega_m >> r\cdot\omega$), and subtracting the resulting average $\left\langle H_{map}\right\rangle_t$ from $H_{map}(\cdot)$ with the following result,

$$\left\{H_1(\bar{J},\bar{\theta},t)\right\}=2\varepsilon\sum_{q=1}^{\infty}H_1(\bar{J},\bar{\theta})\cos(q\Omega_m t)=2\varepsilon\sum_{q=1}^{\infty}\sum_{r\,\varepsilon\,\Re}H_r(\bar{J})\cos(r\cdot\bar{\theta})\cos(q\Omega_m t). \tag{28}$$

Using Eq. (28) and the addition formulas for trigonometric functions leads to the solution of Eq. (27) in the form,

$$S_1(\bar{J},\bar{\theta},t)=\sum_{q=1}^{\infty}\sum_{r\,\varepsilon\,\Re}H_r(\bar{J})\left(\frac{\sin(q\Omega t-r\cdot\bar{\theta})}{r\cdot\omega_o-q\Omega}-\frac{\sin(q\Omega t+r\cdot\bar{\theta})}{r\cdot\omega_o+q\Omega}\right). \tag{29}$$

Use of (i) the canonical transformation equations between old $(J,\theta)$ and new variables $(\bar{J},\bar{\theta})$, (ii) the approximation that $q\Omega_m >> r\cdot\omega_o$, (iii) the interchangeability of the order of the sums in Eq. (29), and, finally, (iv) the separability of the perturbation terms from mapping terms leads to the following explicit first order transformation between variables,

$$J=\bar{J}-\varepsilon\frac{\partial H_1}{\partial\bar{\theta}}\int_{t_n}^{t}(2\pi\delta_{2\pi}(\Omega_m\tau)-1)d\tau, \tag{30a}$$

$$\theta=\bar{\theta}+\varepsilon\frac{\partial H_1}{\partial\bar{J}}\int_{t_n}^{t}(2\pi\delta_{2\pi}(\Omega_m\tau)-1)d\tau. \tag{30b}$$

Evaluating the integrals at the next mapping steps $t_{n+1}$ produces the immediate conclusion $J=\bar{J},\theta=\bar{\theta}$ at the step boundaries (i.e., at each step the mapping Hamiltonian produces actions and angles equal to the and angles associated with the original, physical system).

The preceding conclusions on the relationship between the mapping variables and the system variables is an asymptotic result that is valid over finite time scales. To demonstrate this behavior, Figure 7 shows two orbits in the 12 hr case with eccentricity .7, an inclination of 23°, perigee of 270°, and initial mean anomaly of 70°. The orbit with initial semi-major axis of 26650 km is quasiperiodic, and the orbit with an initial 26620 km semi-major axis is chaotic. Each orbit has been propagated for 10,000 days by both numerical integration and the mapping method. In the upper plot, integrated and mapped results for the quasiperiodic trajectory (with initial semi-major axis of 26650 km) are shown with results that are nearly indistinguishable. The curve in the lower plot represents the difference in the value of their semi-major axes over time, and more clearly demonstrates the slow separation of the trajectories. Clearly, the mapping method correctly depicts the qualitative dynamics, and is quantitatively accurate for a lengthy period. Even after 3000 days, the maximum separation has reached only ~1 km. Again in the upper plot, integrated and mapped results are shown for the chaotic orbit (with initial semi-major axis of 26620 km). The results of these propagations demonstrate the method's ability to correctly reveal the chaotic nature of a trajectory. As expected, the separation of the integrated and mapped trajectories is exponentially divergent. The onset of this divergence takes roughly 7000 days, however, this is not necessarily typical. Other cases (not shown) experience divergence in only a few hundred days. Thus, the method is capable of capturing the qualitative dynamics, but its quantitative accuracy is suspect in chaotic regimes. This is a concern even with highly accurate propagation schemes, and is endemic to propagating chaotic trajectories. Wisdom and Holman[18,19] discuss the numerical stability and accuracy of the mapping at length. The primary consideration in applying Eqs. (25a,b) to obtain qualitatively accurate orbits is to avoid an artificial resonance between the mapping frequency and the natural long period frequencies in the system. When these frequencies are commensurate, *artificial* resonances are created that have the same features as the physical resonances, such as those in Figure 2. If the step size continues to increase, these artifacts can break up to produce a chaotic response. Hence, the step size that is selected must be much smaller than the system natural frequencies (i.e., such as the libration frequency) in order to avoid these artificial behaviors. In practice, a step size of 1 day was usually adequate to produce qualitatively correct results. However, for some circulating orbits this had to be reduced to 1/2 day. In these cases, the KAM surfaces that should appear as lines were 'smeared'; reducing the step size proved effective in eliminating this effect.

One *possible* source for the 'smearing' is thin layer Arnold diffusion. Consider that the mapping method increases the degrees of freedom of the system from 2 to 3 by making the Hamiltonian nonautonomous (time is a new generalized coordinate and the negative of the original Hamiltonian is its conjugate momenta). As discussed earlier, a 3-DOF system admits the possibility of Arnold diffusion. An early paper by Wisdom[20] discusses the possibility of diffusion in the method. Furthermore, he speculates that diffusion is the mechanism causing the formation of the 3/1 Kirkwood gap. He uses the diffusion introduced by the method to expose the physical diffusion process that created the gap. Later he confirms the existence of the physical diffusion process with numerical integration.[21] In the artificial satellite orbit problem, the full dynamical model is 3-DOF, and has been reduced in this study to 2-DOF by ignoring fast period motions. Thus, as with Wisdom's previous work, a diffusion process introduced by the mapping method may reflect a physical diffusion process that could exist in the full dynamic model. Of course, further analysis is required.

Finally, to determine the Poincaré sections easily and efficiently, only the secular component of the perigee rate was retained when appropriate. The approximation is valid as long as the inclination is bounded away from the critical. Below the critical value the secular perigee rate is of order $O(J_2) = O(\varepsilon^{1/2})$, which is an order greater than all of the other oscillations in the problem. Hence, the secular behavior of perigee dominates the response. This fact is confirmed in results from both numerical integration and the mapping method. Of course, for cases at critical inclination the section is determined without utilizing this approximation.

*Results for 12 hr and 8 hr Tesseral Resonance Overlap.* Several Poincaré sections are constructed to verify the results of the analytical and preceding numerical simulations. Figure 8 depicts the section for the 12 hr case with eccentricity of .7 and inclination of 23°. The section represents intersections of the plane defined by semi-major axis $a$ and stroboscopic mean node $\lambda$, when the perigee is equal to 270°. This value of perigee was selected because it places apogee, the slowest portion of the orbit, in the Northern Hemisphere. The figure depicts a variety of structures. Recall Figure 4, in which the anticipated chaotic region appears to originate at a semi-major axis of 26588 km and ends at 26640 km.

The actual maximum width of the chaotic region shown in Figure 8 begins at a semi-major axis of 26584 km and ends at 26644 km for two values of the node, 30° and 210°. Hence the simple analytical argument gets close but underestimates the actual value. The section also depicts additional structures that could not be anticipated using the analytical methods. The figure shows two chaotic 'lobes' that vary as a function of the node. Their maximum widths, stated previously, are near 30° and 210°, and their minimum widths are near 120° and 300°. These results correspond closely to the stable and unstable fixed points predicted for the isolated $V_{3210}$ tesseral harmonic. Inside the strongly chaotic region there still exist small areas of regular quasiperiodic motion. Each 'lobe' contains a small libration region -- these are the remains of the isolated island associated with $V_{3210}$. Hence, even in a large chaotic 'sea', orbits that are regular can still be found. The trajectories will still have large semi-major axis variations since the island structures rotate around the lobe depending on the sampled perigee, however the trajectories are regular and stable (i.e., perturbed motion in the vicinity of the regular orbit remain nearby). Bounding the chaotic region are circulating quasiperiodic orbits, for example, at an initial semi-major axis of 26646 km and node of 0°. The section demonstrates that not only is the type of response dependent on the initial semi-major axis but on initial angles as well.

Now, consider Figure 9, the 8 hr case with .65 eccentricity and inclination of 23°. The section has structures similar to those seen in the previous figure, except that the region of chaos has many more regular regions inside the chaotic sea. The maximum width of the chaotic region is about 38 km, a very close match to the analytical prediction. The large number of regular regions inside the chaotic sea suggest that the resonances are not interacting as strongly as in Figure 8, perhaps because the isolated island centers have a larger separation than in the 12 hr case (Analysis at higher eccentricity show greater island separation and a larger number of stable islands). Several sets of initial conditions are selected to produce regular motion inside the chaotic sea. The trajectories generating the curves are all quasiperiodic, however they have a variety of higher order periods. For instance, the three largest islands near the top of the chaotic region represent a period 3-iterate. That is, each return to the surface produces a point on the island next to the prior intersection with the surface. The circuit is completed every third return. A plot of the orbits trajectory reveals the node is rotating. The three islands enclose a surviving periodic orbit that, itself, closes every third return. On the other hand, the curves that appear near $(a, \lambda)$ equal to (20300 km, 300°) and (20307 km, 330°) represent a period 2-iterate. Its trajectory plot shows the node as well as the semi-major axis are separately periodic, hence librational. The variety of regions in the section indicate that the dynamic responses depend not only on placement of the semi-major axis, but on node placement, as well. Consider two satellites injected with the same semi-major axis (at 20307 km), same perigee (at 270°), same eccentricity (at .65), but different nodes. This scenario is depicted in Figure 10. The satellite orbit with initial node of 343° is chaotic, the other with node of 333° is librating. Note that the initial nodes are dependent on the time of orbit insertion. Both orbits are initially librational in nature, however, at 7000 days the chaotic node transitions to rotation. An immediate conclusion is that orbit insertion, separated by a few degrees, could mean the difference between having a chaotic orbit (and potentially larger stationkeeping costs) and one that is regular.

*Results for Tesseral and Zonal Overlap at Critical Inclination.* As a final illustration consider the case of a satellite orbit near the critical inclination. Figure 3 and Figure 4, the tesseral resonance overlays, show the distance between tesseral resonances decreases with increasing inclination. This indicates that the tesserals coalesce into one resonant term at the exact critical inclination. An additional consequence is that the chaotic region becomes more 'local'. The regions of chaos become isolated to areas near the separatrices of the resonances. This behavior can be seen in Figure 11, that is, a section sampled with perigee at 270°, .72 eccentricity, and an inclination of 55°. Surrounding the inner libration regions is a thin layer chaotic region; this is much reduced from the large sea found in Figure 8. The island structures have become larger. These results suggest that the tesseral resonances are coalescing into one resonance. Finally, Figure 12 shows the Poincaré section in the inclination/perigee plane at critical inclination, and Figure 13 illustrates a sample trajectory near critical inclination. All the initial conditions for the section originate near the unstable fixed point, hence, they exhibit a chaotic response.

Numerical integration is required to produce this figure, because the symplectic mapping method was unable to maintain sufficient accuracy. The resulting section depicts a very localized region of chaos near the former separatrix between libration.. The trajectory plot demonstrates the subtle behavior of chaos in this region. The semi-major axis and node are librating for approximately 5000 days, then suddenly the motion shifts into circulation. Also note the amplitude variations of the semi-major axis are halved.

## Summary

The previous analysis demonstrates the existence of chaotic orbits in the class of resonant orbits that are inclined and eccentric. This conclusion is reached using analytical techniques from secular perturbation theory, results generated from numerical integration, and Poincaré sections obtained using a symplectic mapping technique. The resulting chaotic orbits exhibit semi-major axis variations that are up to six times larger than variations associated with neighboring quasiperiodic orbits. Additionally, orbits in the chaotic region are sensitive to initial conditions. Numerically integrated results demonstrate divergence in the values of the semi-major axes between closely spaced chaotic trajectories is much more pronounced than the divergence in semi-major axis between similarly spaced quasiperiodic trajectories. The Poincaré sections support the conjecture that the regular and chaotic regions are functions of the initial angles. Results from a critically inclined case show that the region of chaos is more localized than in tesseral overlap cases with lower inclinations. A numerical simulation supports the conclusion that the type of chaos found in this region is very subtle. The orbital path can appear quite benign and then suddenly transition into another type of motion. Finally, it is suggested that the complex, nonlinear motions could lead to potentially higher orbit control costs.

## References

1 Fieger, M. E. [1987]. An Evaluation of Semianalytical Theory Against Long Arcs of Real Data for Highly Eccentric Orbits. M.S. Thesis, Massachusetts Institute of Technology, Cambridge, Massachusetts.

2. Frazier, W. [1989]. *Semianalytic Study of High-Eccentricity Orbit Stability and Evolution.* Ph.D. Thesis, University of Colorado, Boulder, Colorado.

3. Khan, M. [1994]. Design of an Optimal Stationkeeping Strategy for a System of Highly Eccentric, High Inclined Orbits. Paper No. 94-109, AAS/AIAA Spaceflight Mechanics Meeting, Cocoa Beach, Florida.

4. Sabol, C., Cefola, P., Metzinger, R. [1995]. Application of Sun-Synchronous, Critically Inclined Orbits to Global Personal Communications Systems. Paper No. 95-222, AAS/AIAA Spaceflight Mechanics Meeting, Albuquerque, New Mexico.

5. Garfinkel, B. [1966]. Formal Solution in the Problem of Small Divisors. *The Astronomical Journal.* **71** (8): 657 - 669.

6. Gedeon, G. S. [1969]. Tesseral Resonance Effects on Satellite Orbits. *Celestial Mechanics* **1**, 167 - 189.

7. Lane, M. T. [1988]. An Analytical Treatment of Resonance Effects on Satellite Orbits. *Celestial Mechanics* **42**, 3 -38.

8. Jupp, A. H. [1988]. The Critical Inclination Problem - 30 Years of Progress. *Celestial Mechanics* **43**, 127 - 138.

9. Hough, M. E. [1979]. *Orbits Near Critical Inclination, Including Luni-Solar Perturbations.* Ph.D. Thesis, Stanford University, Stanford, California.

10. Delhaise, F. and Henrard, J. [1993]. The Problem of Critical Inclination Combined with a Resonance in Mean Motion in Artificial Satellite Theory. *Celestial Mechanics and Dynamical Astronomy* **55**, 261 - 280.

11. Ely, T. A. and Howell, K. C. [1995]. Long Term Evolution of Artificial Satellite Orbits Due to Resonant Tesseral Harmonics. Paper No. AAS-95-196 Space Flight Mechanics Conference, Albuquerque, New Mexico.

12. Goldstein, H. [1980]. *Classical Mechanics*, 2nd ed. Addison-Wesley.
13. Kaula, W. M. [1966]. *Theory of Satellite Geodesy*. Blaisdell.
14. Lane, M. T. [1988]. An Analytical Treatment of Resonance Effects on Satellite Orbits. *Celestial Mechanics and Dynamical Astronomy* **42**, 3 - 38.
15. Lichtenberg, A. J. and Liebermann, M. A. [1992]. *Regular and Chaotic Dynamics*, 2nd ed. Springer-Verlag.
16. Escande, D. F. and Doveil, F. [1981]. Renormalization for Computing the Threshold of the Large-Scale Stochastic Instability in Two Degree of Freedom Hamiltonian Systems. *Journal of Statistical Physics* **26** (2), 257 - 284
17. Chao, C. and Schmitt, D. [1989]. Eliminating GPS Stationkeeping Maneuvers by Changing the Orbit Altitude. Paper No. 89-407, AAS/AIAA Astrodynamics Specialist Conference, Stowe, Vermont.
18. Wisdom, J. and Holman M. [1991]. Symplectic Maps for the N-Body Problem. *The Astronomical Journal* **102** (4), 1528 - 1538.
19. Wisdom, J. and Holman, M. [1992]. Symplectic Maps for the N-Body Problem: Stability Analysis. *The Astronomical Journal* **104** (4), 2022 - 2029.
20. Wisdom, J. [1982]. The Origin of the Kirkwood Gaps: A Mapping for Asteroidal Motion Near the 3/1 Commensurability. *The Astronomical Journal* **87**(3), 577 - 593.
21. Wisdom, J. [1983]. Chaotic Behavior and the Origin of the 3/1 Kirkwood Gap *Icarus* **56**, 51 - 74.
22. Wiesel, W. [1989]. *Spaceflight Dynamics*. McGraw Hill

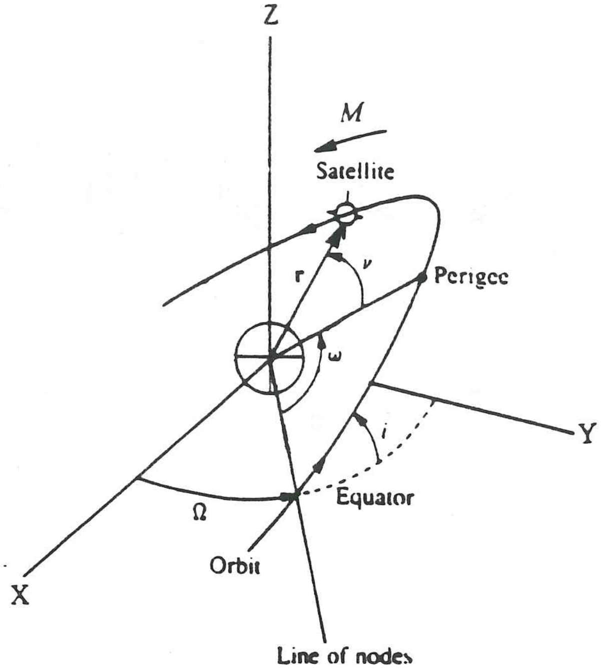

Figure 1: Earth-Centered orbit geometry [22].

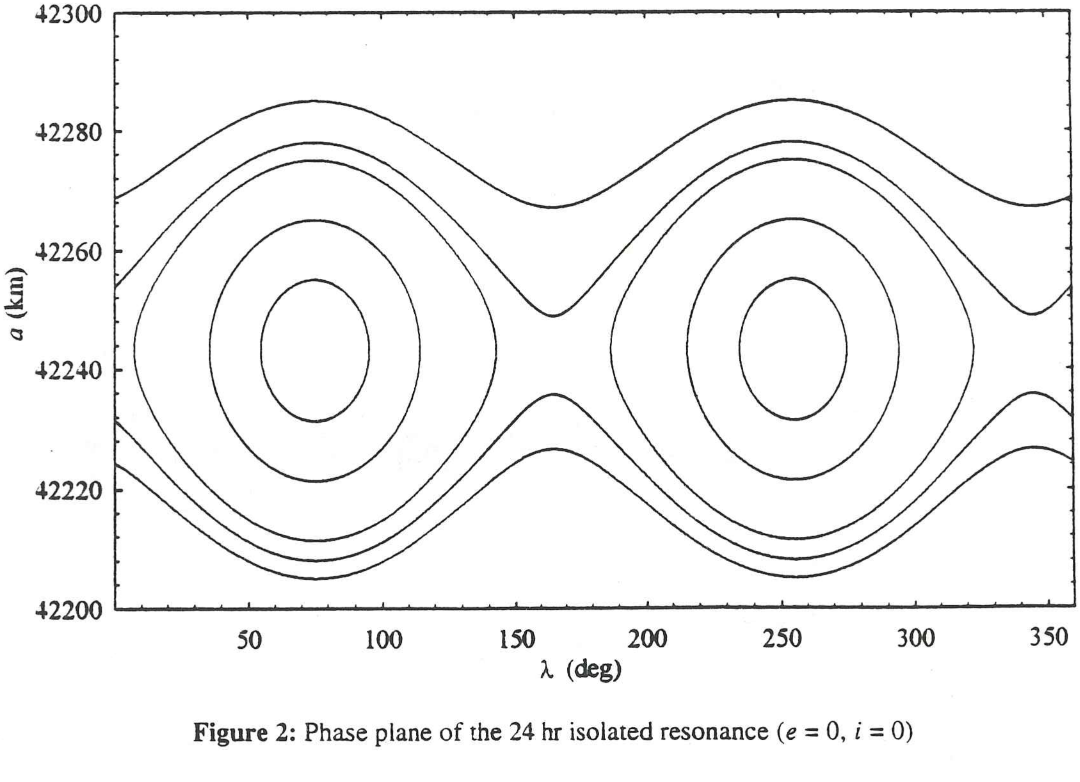

**Figure 2:** Phase plane of the 24 hr isolated resonance ($e = 0$, $i = 0$)

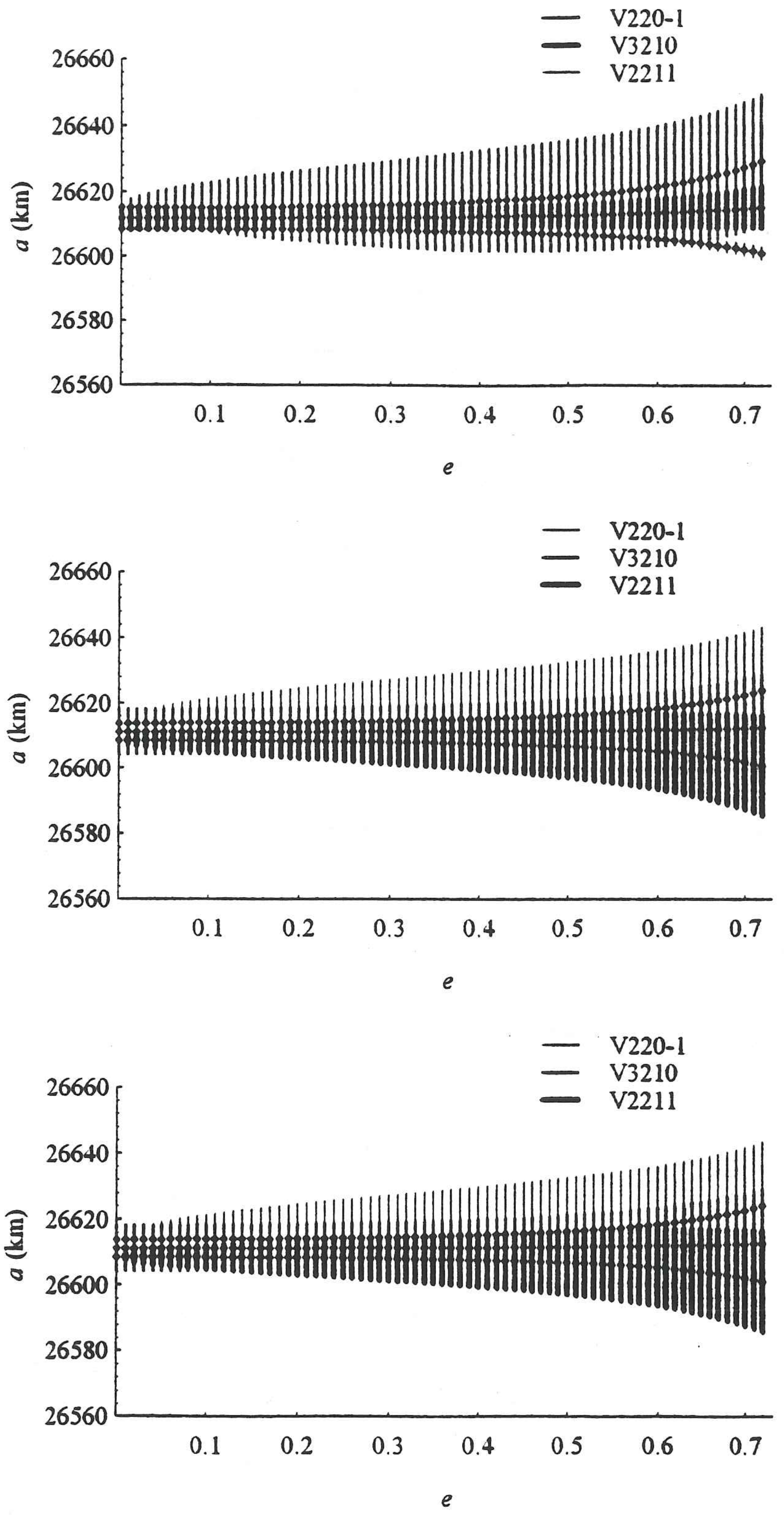

**Figure 3:** Overlay of Critical Harmonics for the 12 hr orbits at $i$ = 3° (top), 23° (middle), 55° (bottom)

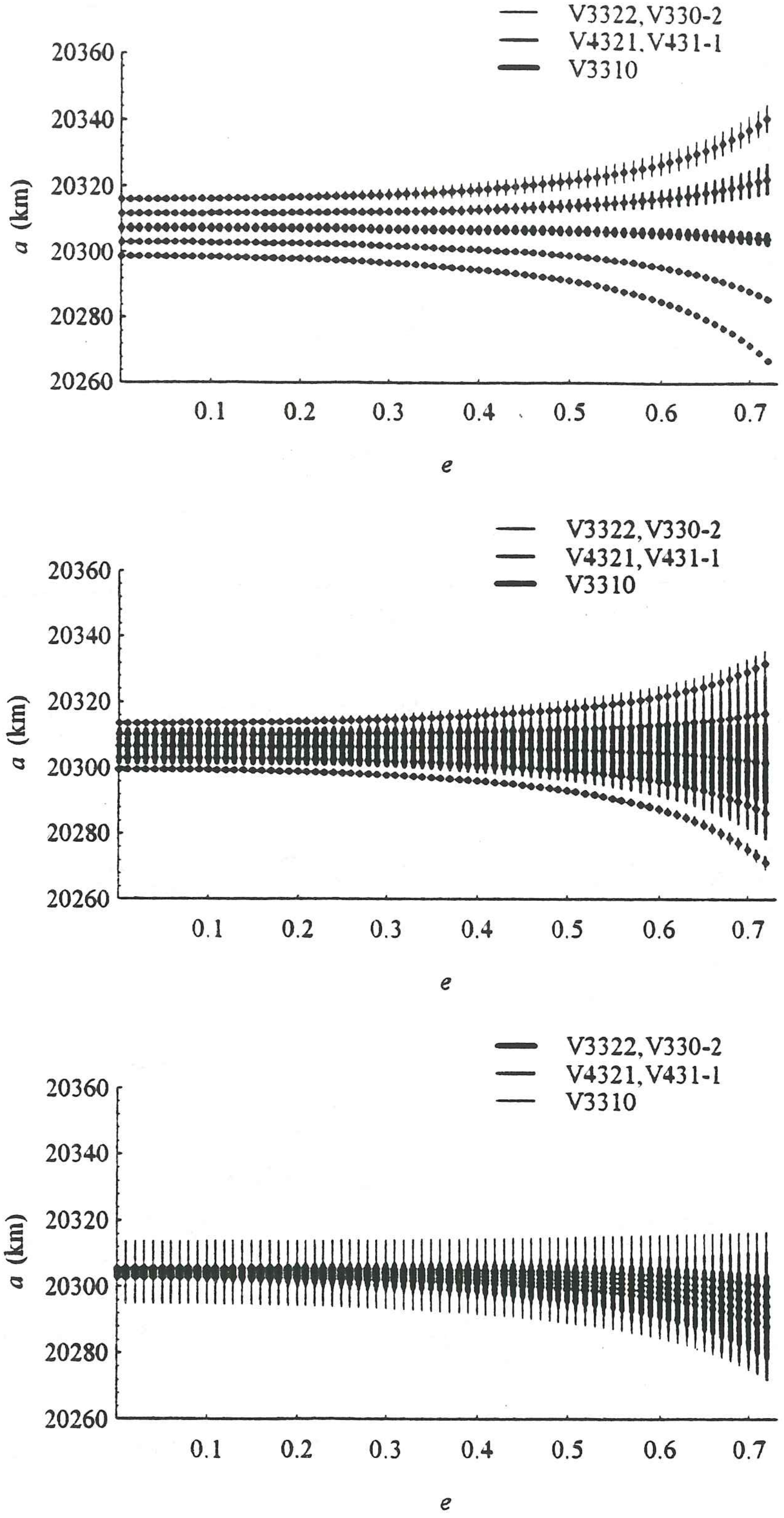

**Figure 4:** Overlay of Critical Harmonics for the 8 hr orbits at *i* = 3° (top), 23° (middle), 55° (bottom)

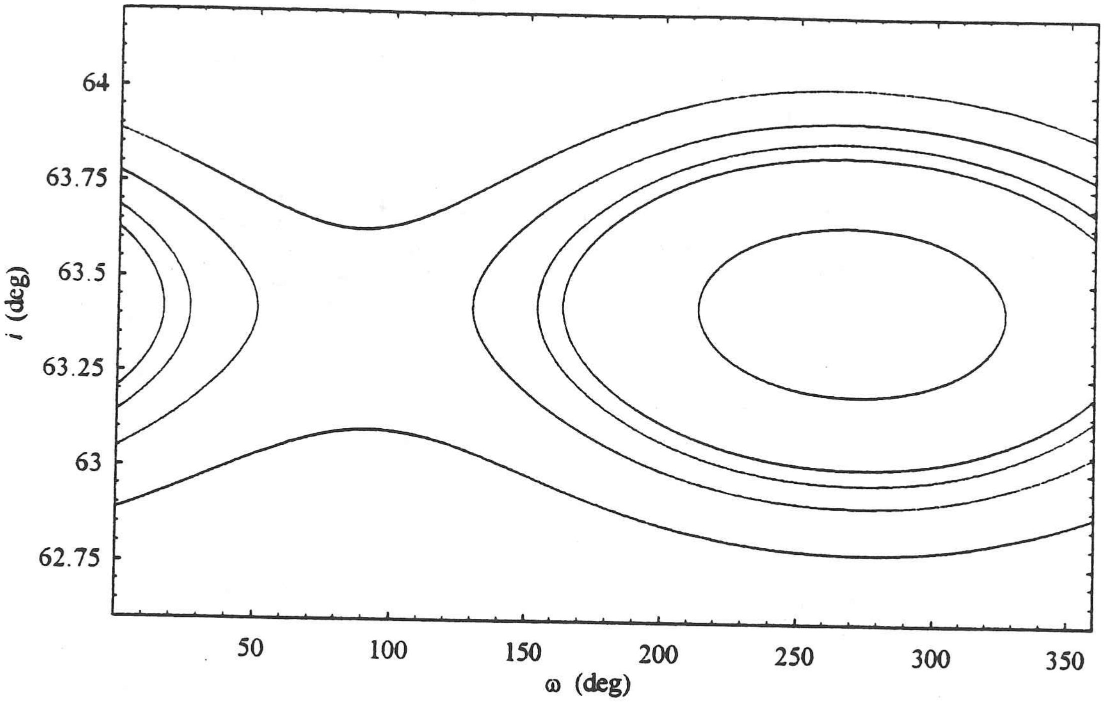

**Figure 5:** Inclination/perigee phase plane for 12 hr orbits at critical inclination ($a$ = 26700 km, $\lambda$ = 100°)

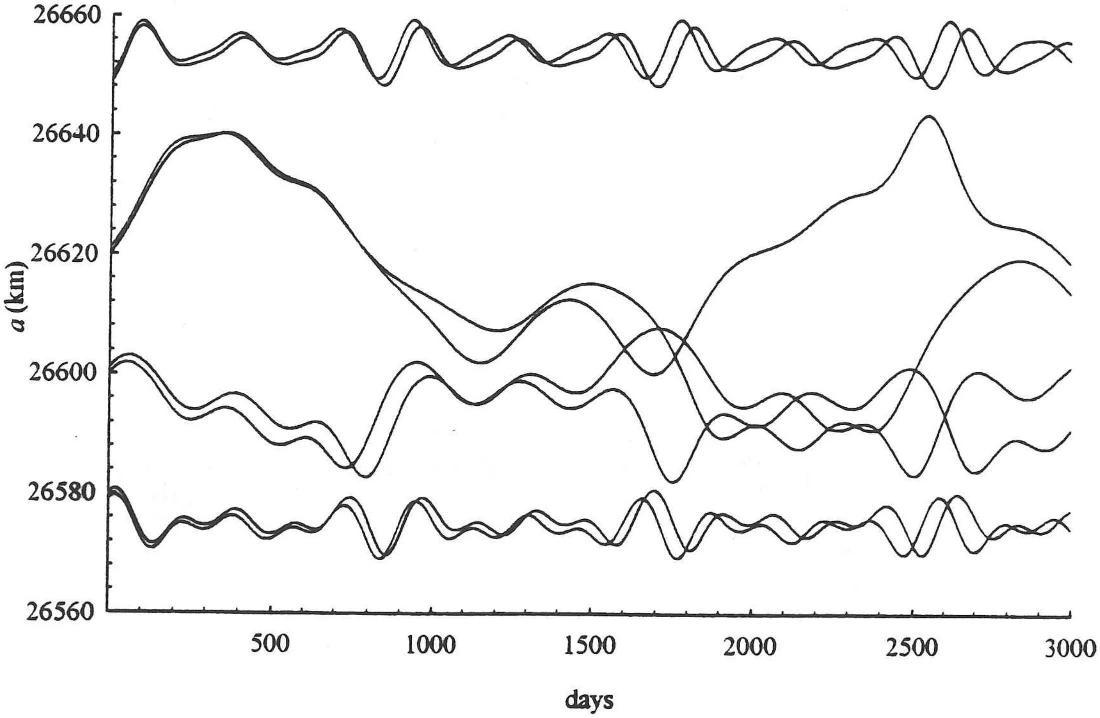

**Figure 6:** 12 hr orbit; semi-major axes in resonance overlap region ($e$ = .7, $i$ = 23°)

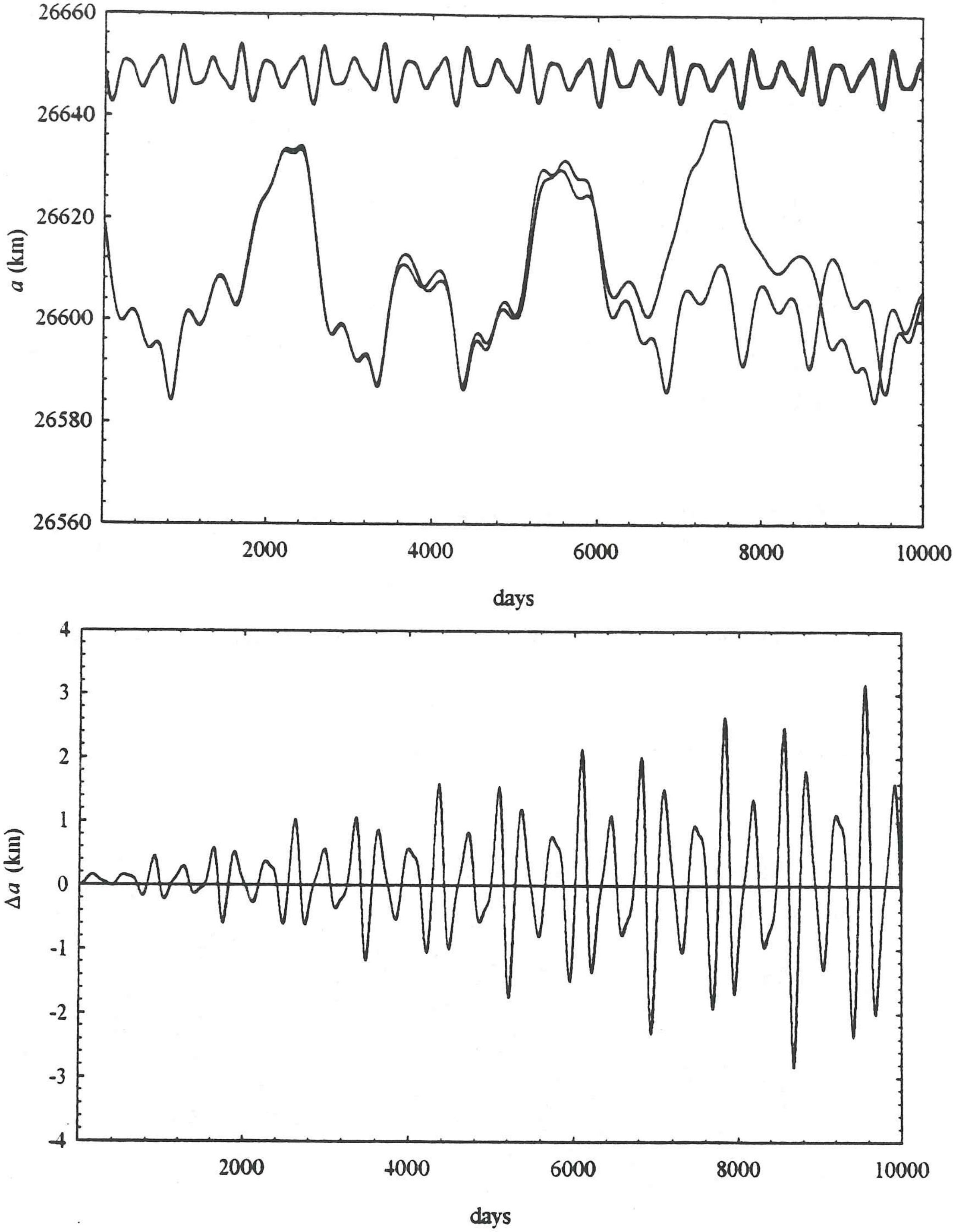

**Figure 7:** Comparison of mapping method with numerical integration for a quasiperiodic and chaotic orbit. The upper plot shows semi-major axis versus time for both orbits, both methods. The lower plot is the difference between the numerically integrated semi-major axis with the mapping result in the quasiperiodic orbit.

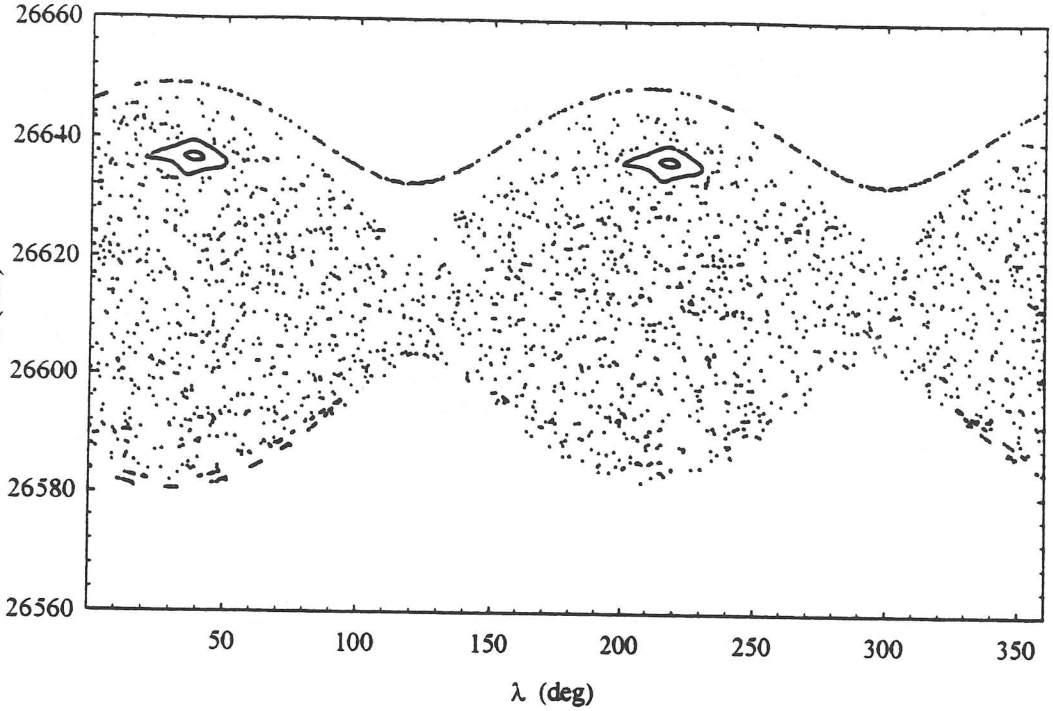

**Figure 8:** Poincaré section of 12 hr resonance overlap region ($e = .7$, $i = 23°$, $\omega = 270°$)

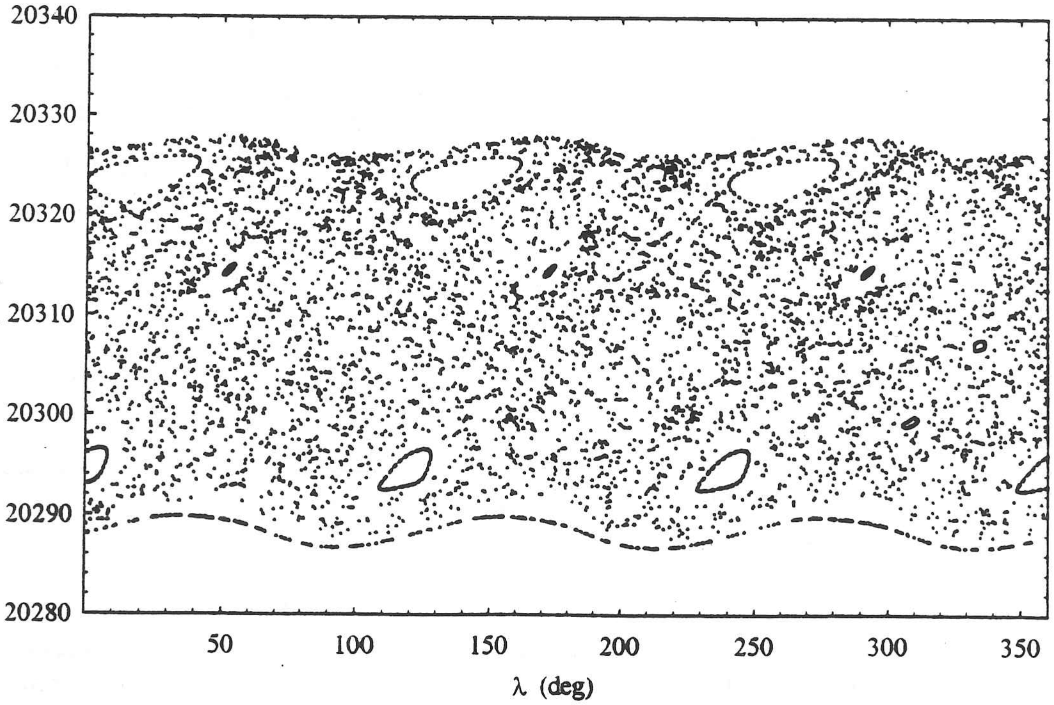

**Figure 9**: Poincaré section of 8 hr resonance overlap region ($e = .7$, $i = 23°$, $\omega = 270°$)

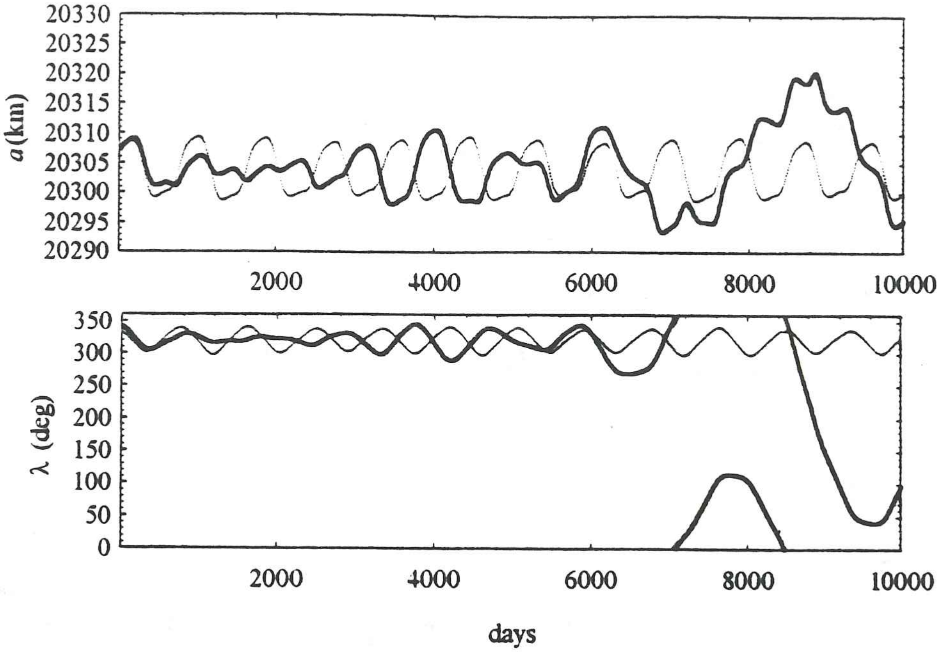

**Figure 10**: Two 8 hr orbits ($a = 20307$ km, $e = .65, i = 23°$). The thin line represents a trajectory in a libration region ($\lambda = 333°$). The thick line represents a trajectory in a neighboring chaotic region ($\lambda = 343°$).

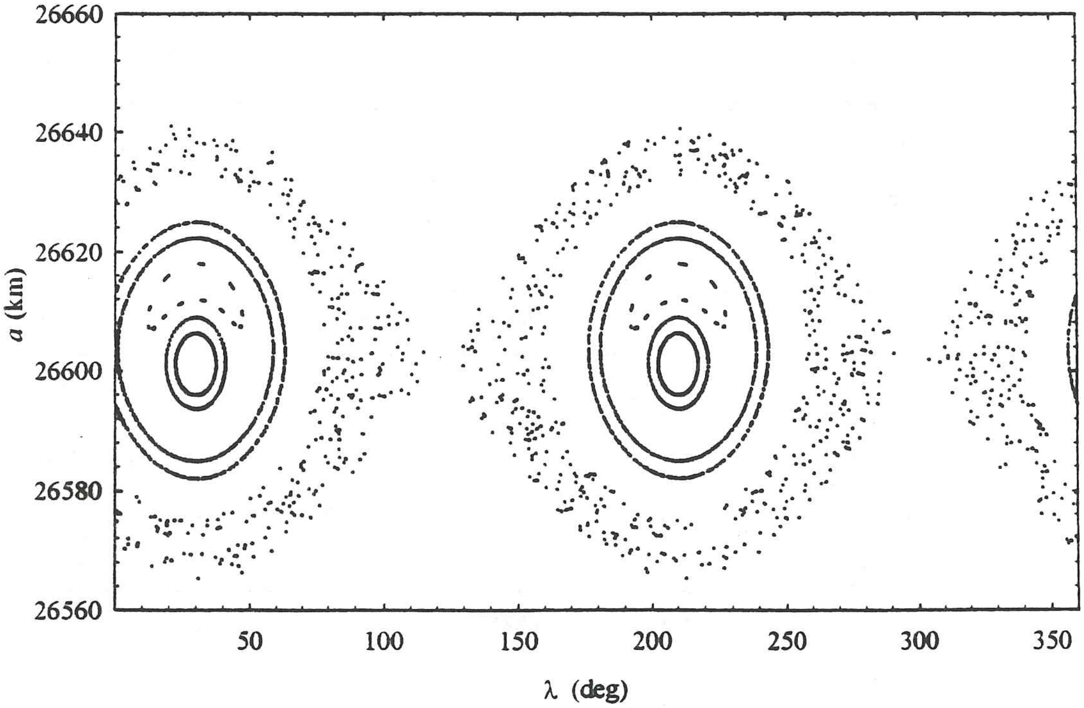

**Figure 11:** Poincaré section of 12 hr resonance overlap region ($e = .72$, $i = 55°$, $\omega = 270°$)

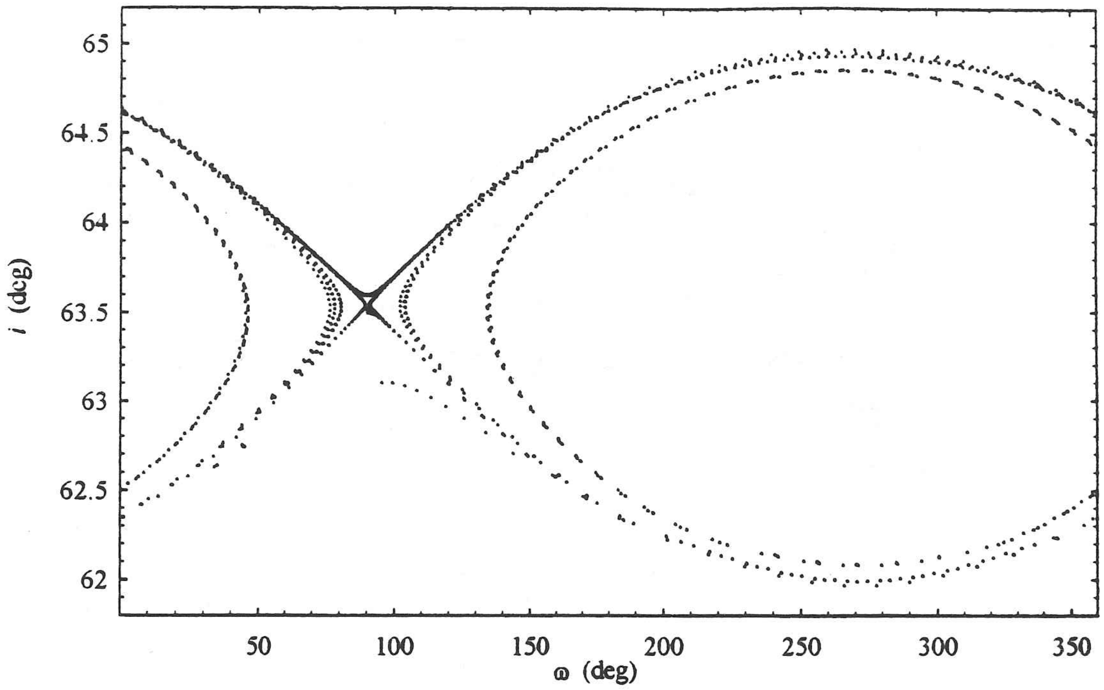

**Figure 12:** Poincaré section of 12 hr resonance overlap at critical inclination (*a*=26595.5, λ = 200°)

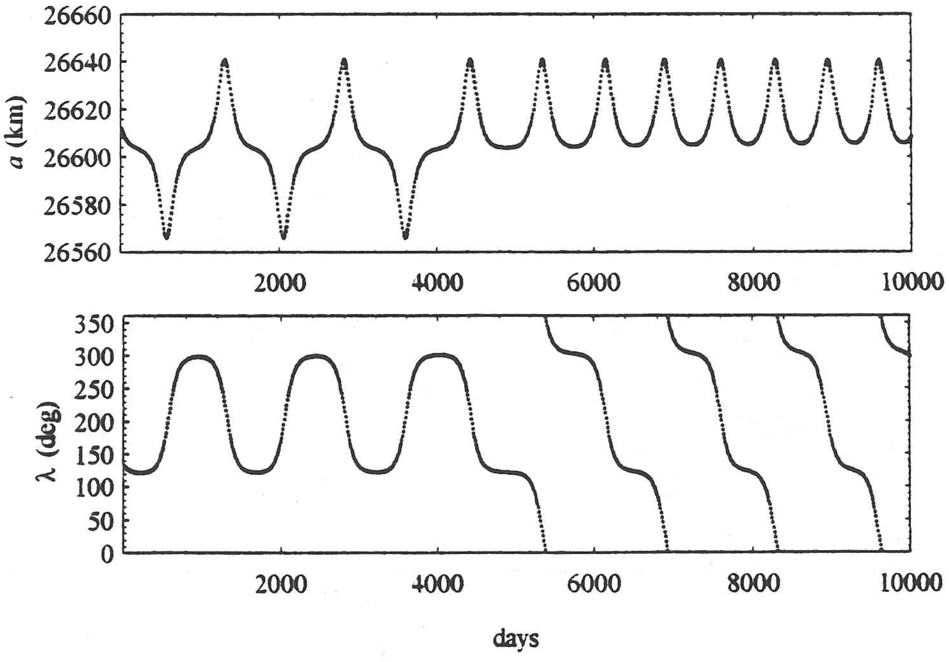

**Figure 13:** 12 hr orbit near critical inclination (*a* =26613.3 km, *e* = .7, *i* = 63.2°, ω = 270°, *M* = 0°)